Xiangjia Li
Daniel J. Epstein Department of Industrial and
Systems Engineering,
University of Southern California,
Los Angeles, CA 90089
e-mail: xiangjil@usc.edu

Huachao Mao
Daniel J. Epstein Department of Industrial and
Systems Engineering,
University of Southern California,
Los Angeles, CA 90089
e-mail: huachom@usc.edu

Yayue Pan
Assistant Professor
Department of Mechanical and Industrial
Engineering,
University of Illinois at Chicago,
Chicago, IL 60607
e-mail: yayuepan@uic.edu

Yong Chen[1]
Professor
Daniel J. Epstein Department of Industrial and
Systems Engineering,
Department of Aerospace and Mechanical
Engineering,
University of Southern California,
Los Angeles, CA 90089
e-mail: yongchen@usc.edu

Mask Video Projection-Based Stereolithography With Continuous Resin Flow

The mask image projection-based stereolithography (MIP-SL) is a low-cost and high-resolution additive manufacturing (AM) process. However, the slow speed of part separation and resin refilling is the primary bottleneck that limits the fabrication speed of the MIP-SL process. In addition, the stair-stepping effect due to the layer-based fabrication process limits the surface quality of built parts. To address the critical issues in the MIP-SL process related to resin refilling and layer-based fabrication, we present a mask video projection-based stereolithography (MVP-SL) process with continuous resin flow and light exposure. The newly developed AM process enables the continuous fabrication of three-dimensional (3D) objects with ultra-high fabrication speed. In the paper, the system design to achieve mask video projection and the process settings to achieve ultrafast fabrication speed are presented. The relationship between process parameters and the surface quality of the built parts is discussed. Test results illustrate that the MVP-SL process with a continuous resin flow can build three-dimensional objects within minutes, and the surface quality of the fabricated objects is significantly improved. [DOI: 10.1115/1.4043765]

Keywords: additive manufacturing, stereolithography, mask video projection, continuous resin flow, high-speed fabrication

1 Introduction

Additive manufacturing (AM) provides a promising fabrication solution to quickly customize products with complex shapes, which cannot be achieved by traditional manufacturing processes [1]. Various AM processes have been developed for a diverse range of materials including metal, polymer, ceramics, and composites [2,3]. The main difference between these AM processes is how layers of materials are deposited to form three-dimensional (3D) objects [1,2]. Based on the material deposition methods, additive manufacturing processes can be divided into two main categories: one is to deposit materials based on moving a small point (or multiple points) along controlled paths to form a layer such as material extrusion, material jetting, powder bed fusion, and selective laser melting [4]; and another is to deposit materials simultaneously to form the whole layer using surface-based energy control mechanisms such as photopolymerization [2,5]. The mask image projection-based stereolithography (MIP-SL) is developed based on the photopolymerization that turns photocurable resin from liquid into solid using controlled light exposure of a two-dimensional (2D) area [6–8].

As AM technology evolves, more and more applications have been found in various fields including industrial design and manufacturing, biomedical engineering, and aerospace [1,2]. For applications in optics, fluid, electronics, and biotissue engineering, smooth surface is important in order to achieve desired functional performances [2,9,10]. However, most of the additive manufacturing methods are layer-based processes, where a computer-aided design (CAD) model is sliced into hundreds of 2D layers and materials are deposited to the final shape through a set of 2D layers [4,11]. Obvious stair-stepping effect exists on the surfaces of the fabricated objects, which has an adverse impact on the performance of 3D-printed parts. Many techniques have been developed before AM processes to improve the surface quality of 3D objects that are built in layers [6,7,12–15].[2] For example, a meniscus equilibrium method for the fabrication of smooth surface has been developed earlier [6,7,12]. The key idea of the approach is to cure liquid meniscus generated by surface tension at the corners of intersecting planes to form curved surfaces after the fabrication of multiple layers. Compared with the traditional layer-based fabrication process, a much smoother surface can be achieved [6]. Instead of curing liquid meniscus in the building process, a method has been developed by Luxexcel to achieve smooth surface fabrication of optical lenses.[3] The method is based on the natural surface tension of material to form smooth optical surface after the deposition of the polymer liquid droplet.[4] Although the surface quality has certain improvements, the aforementioned 3D printing methods are still limited on the fabrication efficiency and accuracy.

Recently, a broad range of layer-less 3D printing technologies has been developed that can continuously deposit and solidify material [14–22]. For example, a continuous liquid interface production (CLIP) process was presented that can achieve an order of magnitude faster building speed and better surface quality [16]. The CLIP process is based on a special transparent and permeable window that allows both light and oxygen to get through [16]. Another AM process based on computer numerical control was developed to fabricate smooth structures, in which the material is continuously cured along with the movement of the light tool by

---

[1]Corresponding author.

Manuscript received November 24, 2018; final manuscript received May 7, 2019; published online June 13, 2019. Assoc. Editor: Sam Anand.

[2]https://www.luxexcel.com/ophthalmic-technology/ophthalmic-lenses
[3]See Note 2.
[4]See Note 2.

photopolymerization [14,15]. To further improve fabrication resolution, a light guide tool, which can project two-dimensional (2D)-patterned light beam, was developed by immersed surface accumulation process (ISAP) [20]. Based on the high resolution of 2D-patterned light beam, microscale features can be continuously fabricated using ISAP [23]. However, even though the fabrication efficiency and the surface quality have been improved by the newly developed layer-less AM processes, there are still several limitations that required being addressed [24]. One of the most critical limitations is the cross-sectional area that can be continuously fabricated. For example, to maintain a certain fast printing speed, the CLIP process can only fabricate the object composed of hollow structures, of which the cross-sectional area is relatively small [16,25]. How to address the surface area limitation in the continuous MIP-SL process is an open question that requires to be addressed by the AM research community.

In this paper, we present a novel layer-less AM process that can have less constraint on cross-sectional areas while achieving continuous fabrication with improved building speed and surface quality. We extended the MIP-SL process to the mask video projection-based stereolithography (MVP-SL) process, in which the shape of a CAD model can be directly fabricated using a high frame rate video. That is, the 2D-patterned light beam is continuously projected through a digital micromirror device (DMD) using a frame rate of 30–120 images per second (similar to the CLIP and ISAP processes). During the fabrication process, such high-frequency mask image projection makes the continuous fabrication in the stereolithography process possible. However, different from the CLIP and ISAP process, we integrated a continuous side motion (in the X-axis) between the resin tank and the Z platform to actively feed resin to the light exposure area [26]. Hence, the resin recoating can be significantly accelerated to catch up with the crosslinking speed of the photocurable polymer. More importantly, the side motion speed can be actively controlled. This is dramatically different from the passive resin feeding strategy used in the CLIP and ISAP processes, which relies on the pressure difference between the photocuring area and the environment, and hence, the feeding rate is limited. In the paper, we first analyze the mathematical model of the liquid filling problem in the MVP-SL process. Based on it, the surface area fabrication capability of the MVP-SL process and the related process parameters are discussed. Due to the integrated side movement that can speed up the resin recoating process, the MVP-SL with a continuous resin flow (MVP-SL$_{CRF}$) can achieve an improved fabrication speed for CAD models with large cross-sectional areas. Experiments conducted on some test cases demonstrated that MVP-SL$_{CRF}$ can achieve a fabrication speed over 10 mm/min in general. Similar to the CLIP process, the surface quality of MVP-SL$_{CRF}$ is significantly improved without any stair-stepping effect that is typical for the layer-based stereolithography process. At the same time, some limitations of MVP-SL$_{CRF}$ are also discussed that need to be addressed in future research.

2 Process Characterization of MVP-SL

Two design configurations exist in the stereolithography process. One design configuration is the top–down-based layout, in which light is projected down in the Z-axis and liquid resin is recoated by free surface flow or an external blade to recoat a thin layer of resin. Various recoating methods have also been developed to recoat high viscous liquid resin with desired layer thickness such as ultra-sound vibration, tilted angles, and doctor blade [27–29]. Another design configuration is the bottom-up-based layout, in which light is projected up from the bottom of the resin tank, and the building platform is moved up in order to fill a thin layer of liquid resin for layer fabrication. However, a large tank with filled resin is required to keep the printed part merged inside the resin tank [27,28]. Hence, the bottom-up design configuration is studied in the MVP-SL$_{CRF}$ process, in which a flat and clear glass

tank is mounted on a rotary stage (refer to Fig. 1(a)). One significant challenge of this design layout is how to separate the newly cured layer from the surface of the resin tank by overcoming a large attaching force between them [30]. Similar to our previous study [26], a 2 mm thickness PDMS (Sylgard 184, Dow Corning) layer is coated on the glass tank. Due to the permeation of oxygen through the coated PDMS layer, the resin is prevented to be directly cured on the PDMS layer and a thin oxygen inhibition layer of non-polymerization liquid resin is formed between the PDMS and the newly cured layer [31]. Hence, the cured layer can be easily slid along the side direction (in the X-axis).

2.1 Curing Performance of Material. To set an appropriate printing speed V_z, we need to first understand the cure depth of the liquid resin that is used. Based on the polymerization principle, Jacobs presents a mathematical model of cure depth C_d with exposure energy E_c and penetration depth D_p as shown in the following equation [32,33]:

$$C_d = D_p \ln\left(\frac{E_{\max}}{E_c}\right) \tag{1}$$

The projection extent of our MVP-SL$_{CRF}$ process is set to be 50 × 37.5 mm^2; accordingly, the light intensity of a focused image is measured as 30 mw/cm^2. Under the energy of full light exposure, the cure depth of liquid resin SI500 (from Evsiontec, Ferndale, MI) is 150 μm. When the value of the continuous printing speed is half of the cure depth of the photocurable resin, the surface quality of built models is not acceptable due to overcured features. However, when the continuous printing speed is much faster than the cure depth of the used photocurable resin, there are gaps on the surface of built models because the light energy is not sufficient to fully photopolymerize liquid resin based on such a continuously moving-up speed. A series of resin refilling and curing experiments were conducted to determine the continuous printing speed V_z with the best surface quality. Based on the experiments, we found that k_z can be set in the range of 0.9–1.2 depending on the mechanical strength that is required in the built object. That is,

$$V_Z = k_z C_d \tag{2}$$

The mechanical strength of the photocured polymer has a relation with the polymer's crosslinking level [4]. The mechanical strength of the 3D-printed parts turns to be larger with a smaller value setting k_z, because the mechanical strength of the fabricated part is increased with higher crosslinking level of the polymer after receiving increased light exposure with a slower continuous moving-up speed V_Z (Table 1).

Based on the material continuous printing property and the energy distribution of the projection light, the cure depth of liquid resin can be further controlled by adding photoinitiator or light absorber in the used resin, which makes it possible for a built object to achieve a large range of mechanical strength [32]. Based on Eq. (2), with sufficient material refilling, the continuous printing speed is only determined by the curing property of the resin. However, for layers with large cross-sectional areas, the liquid refilling speed cannot meet the requirements of high-speed continuous printing. To figure out the limitation of liquid filling in MVP-SL, we studied the mathematical model of liquid filling

Table 1 The mechanical strength of material fabricated by using different Kz

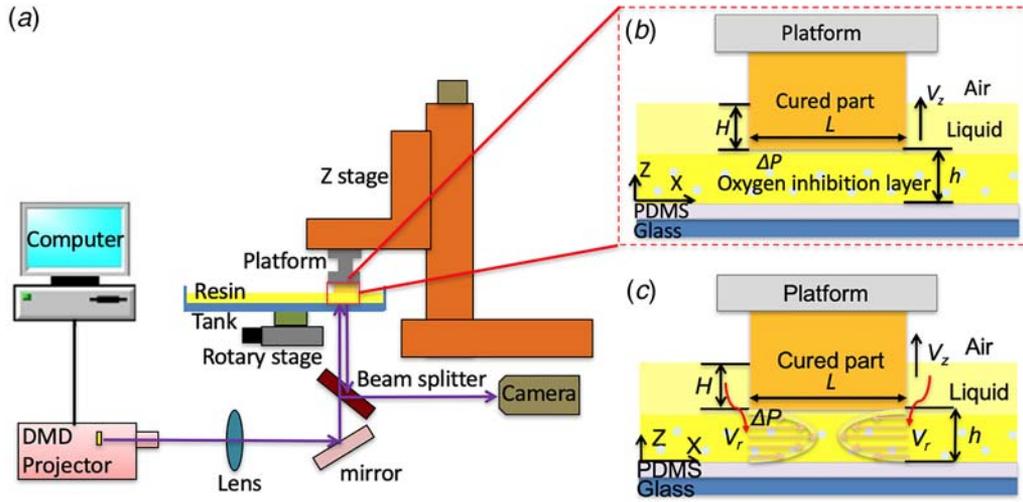| K_z	Young's modulus (E) (MPa)
0.9	81–108
1	58–72
1.1	38–45
1.2	5–7

Fig. 1 An illustration of the material recoating with directly continuous Z movement: (a) the schematic diagram of MVP-SL, (b) an illustration of the recoating process with directly continuous Z movement, and (c) an illustration of resin recoating of continuous resin flow with directly continuous Z movement

in MVP-SL and conducted designed experiments to verify the liquid filling assumption, which are presented in the following section.

2.2 Modeling of Liquid Filling in MVP-SL. In the bottom-up–based MVP-SL process, due to the coated PDMS film on the surface of glass tank, a certain amount of oxygen can permeate through the PDMS layer, which generates an oxygen inhibition layer on the surface of PDMS that enables the continuous fabrication of 3D objects (refer to Fig. 1(b)) [16,31]. We first analyze the relationship between the liquid filling time t, the side length of cured part L, and gap distance h (refer to Fig. 1(c)). Assume the surfaces of the cured layers and the PDMS layer is parallel and the resin flow can be treated as the Hele-Shaw flow [34]. The liquid flow below the cured part can be considered fully developed, without time disturbance, and incompressible, and the velocity of the resin in the Z direction satisfies the following equation:

$$v_r = \frac{\Delta p}{\mu L}\left[\left(\frac{h}{2}\right)^2 - \left(z - \frac{h}{2}\right)^2\right] \tag{3}$$

where ΔP is the local pressure difference, Z is the distance in the perpendicular direction, μ is the viscosity of the liquid resin, and v_r is the velocity in the direction of x_i. Suppose liquid resin only flows in the channel generated by the oxygen inhibition layer, where h is 2.5 μm (for the coated PDMS film), viscosity of the resin μ is 180 cP at 30 °C, the standard atmospheric pressure is 101,325 Pa, the height of the resin H is 20 mm, and the density of the resin ρ is 1.10 g/cm^3. The speed of filling resin can be calculated based on Eq. (3). Hence, the mean resin refilling speed driven by the resin gravity and the air pressure is around 0.570 mm/s. However, in the layer-less additive manufacturing process with continuous video projection, the liquid resin is exposed to the projection light during its filling process. Due to the polymerization process, the viscosity increases exponentially in the monomer conversion process [32,33]. To illustrate the filling dynamics in the continuous photopolymerization process, we use a simplified exponential function to describe the viscosity profile of the liquid in the gap. Hence, Eq. (3) could be modified as follows:

$$v_r = \frac{\Delta p}{\mu e^k L}\left[\left(\frac{h}{2}\right)^2 - \left(z - \frac{h}{2}\right)^2\right] \tag{4}$$

where k is a constant. If the liquid does not absorb light energy, k is zero; otherwise, it is a nonzero constant. Consequently, the refilling speed v_r will further decrease along with the increase of the viscosity due to the continuous photopolymerization. Based on the aforementioned calculation, we can see the self-filling speed of resin driven by the gravity, and air pressure is rather slow; consequently, only microscale features can be continuously fabricated. In the CLIP process, a special permeable window instead of a PDMS film was used that can increase h to a much larger value (around 100 μm) [16]. Hence, the CLIP process can achieve the continuous fabrication of features with a relatively larger area; however, the maximum area is still quite limited [16].

In the MVP-SL fabrication process, where the liquid resin is continuously exposed to light irradiation during the resin filling process, the approximate flow rate of the liquid resin under the cured part with square section area L^2 can be predicted as follows:

$$Q = \int_0^L dy \int_0^h \frac{\Delta p}{\mu e^k L}\left[\left(\frac{h}{2}\right)^2 - \left(z - \frac{h}{2}\right)^2\right] dz \tag{5}$$

The refilled liquid resin will be cured along with the movement of curing platform with the speed V_z. In a unit time, the newly cured resin is equal to the amount of resin that reaches the fabrication area, and then, the valid side length L_r of the cured part built with sufficient resin refilling can be calculated with given V_z as follows:

$$L_r = \left(\frac{2\Delta p h^3}{3\mu e^k V_z}\right)^{\frac{1}{2}} \tag{6}$$

To verify the above resin refilling assumption, we performed a set of experiments to identify the relation between the side length of the valid fabrication area L_r and the continuous printing speed V_z in the Z-axis. A series of cubes with different cross-sectional areas ranging from 0.01 mm^2 to 4 mm^2 were fabricated using the MVP-SL process with different printing speed V_z (refer to Figs. 2(a) and 2(b)). We consider a fabricated model to be failed when there are air bubbles or shadows inside the cross-sectional areas of the fabricated objects (Fig. 2(c)); instead, if no bubbles or shadows of resin were observed inside the 3D-printed parts, we would consider the continuous fabrication settings valid for the given cross-sectional areas (Fig. 2(d)). Based on the experimental results, we further identify critical values of valid continuous fabrication settings based on different printing speed V_z from 30 μm/s to 150 μm/s. The analyzed experimental results with valid continuous
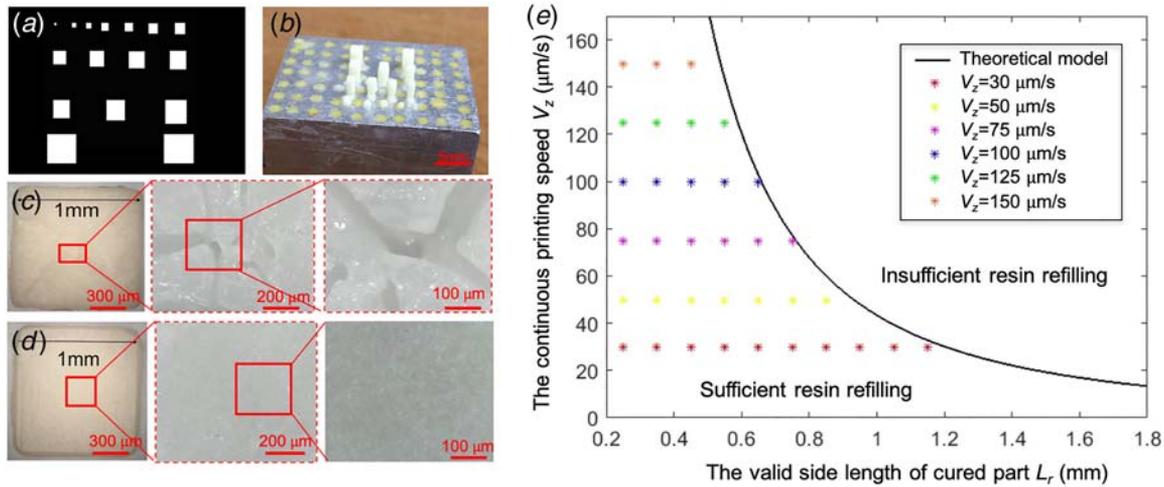
Fig. 2 Fabrication results of cubes with different dimensions with self-refilling resin under gravity and air pressure: (a) a frame image of the projection video, (b) printed cubes using the MVP-SL process, (c) a fabricated cube with insufficient resin refilling and microscope image of the cross section of the fabricated cube with insufficient resin refilling, (d) a fabricated cube with sufficient resin refilling and microscope image of the cross section of the fabricated cube with sufficient resin refilling, and (e) the side length of valid fabrication area with self-refilling resin under different moving speed V_z in the Z-axis

fabrication settings are shown in Fig. 2(e), which only considers liquid resin refilling that is driven by the gravity and the ambient air pressure.

Under the boundary line shown in Fig. 2(e), all of the models are located in the valid region, which can be continuously fabricated using the MVP-SL process with self-refilled resin. Based on the results shown in Fig. 2(e), we can see that the side length of the valid fabrication area L_r turns to be bigger as the continuous printing speed V_z decreases. When the side length of the cured part S is larger than the side length of the valid fabrication area L_r associated with certain printing speed V_z, bubbles would appear in the center portion of the built layers because fresh liquid resin cannot completely refill the gap during the photocuring time. In such a situation, the continuous printing process will require more waiting time in order for the liquid resin to fully refill the gap. Hence, a larger area A can be achieved only by slowing down the printing speed V_z. In our experiments, the printing speed V_z had to be reduced to be smaller than 5 μm/s in order to fabricate a cross-sectional area A of which the side length is larger than 2 mm. To achieve the MVP-SL process with a faster continuous fabrication speed (i.e., an increased V_z), it is desired to quickly fill sufficient resin in the formed gap during the fabrication process. Consequently, instead of relying only on the self-refilling driven by the gravity and the ambient air pressure, other resin refilling mechanisms need to be explored in order to achieve the continuous fabrication of a much larger cross-sectional areas.

3 MVP-SL Process With Continuous Resin Flow

Resin refilling driven by the gravity and the ambient air pressure can only enable the MVP-SL process to achieve microscale continuous fabrication. As shown in our previous study on the MIP-SL process [26], the liquid resin recoating problem can be addressed by adding a side motion. Inspired by the idea, we present a rotational two-way movement to achieve the continuous resin flow in the MVP-SL process. Figure 3(a) shows the principle of the continuous resin recoating method based on the two-way movements in both the Z- and X-axes.

3.1 Continuous Resin Flow Design.
When the stage with the tank moves left with speed V_x, the liquid resin filled the gap between the cured layers and the PDMS surface with corresponding speeds in the horizontal direction (i.e., in the X-axis); and at the same time,

the Z stage elevated the platform with a set speed V_z. The sliding movement in the X direction could accelerate the resin flow to ensure that there is sufficient resin for the continuous mask image projection. Hence, a two-way movement can be applied in the MVP-SL process to actively refill resin to achieve the continuous fabrication of macroscale objects. Therefore, during MVP-SL$_{CRF}$, the Z stage is continuously moved up with a controlled speed V_z, and at the same time, the X linear stage on which the resin tank is mounted is continuously moved with a suitable moving speed V_x, which is decided by the cross-sectional area of the model. Note that, during the two-way movement process, there is no relative motion between the platform and the projection device (refer to Fig. 3(a)). Therefore, the continuously photocured material can be exactly attached to the previous layers using a video that can be precomputed based on V_z. By continuously moving the tank left Δx in the X direction, we aim to ensure sufficient resin refilling in the cross-sectional area of the built model in the MVP-SL process. To achieve the goal, it is critical to figure out the appropriate value of each parameter. In the MVP-SL$_{CRF}$ process, there are four critical parameters that need to be carefully considered: cure depth of the material C_d, the printing speed V_z, the speed of side movement V_x, and the cross-sectional area A of a model to be fabricated by the MVP-SL process.

3.2 Modeling of Continuous Resin Flow.
Liquid resin during the refilling flow based on an additional X-axis movement can still be regarded as isothermal and incompressible fluid since the platform surface is parallel to the PDMS surface. Since the refilling gap is small (in μm), we can assume that the liquid flow around cured portion is stable without turbulence. The momentum equation for the Newton flow in the system can be written as follows [34–36]:

$$\rho \frac{D\vec{v}}{Dt} = \vec{F} - \nabla p + \nabla \cdot \tilde{\tilde{\tau}} \qquad (7)$$

where ρ, $\vec{v}$, $\vec{F}$, ∇p, and $\tilde{\tilde{\tau}}$ are density, velocity, body forces, pressure gradient, and stress tensor, respectively. Based on Eq. (7), in the MVP-SL$_{CRF}$ process, resin refilling speed is determined by moving force and positive pressure gradient including the resin gravity and the air pressure. Hence, the filling flow between the cured layers and the PDMS surface can be considered as the Couette flow (refer to Fig. 3(b)) [36,37]. With fresh liquid streaming
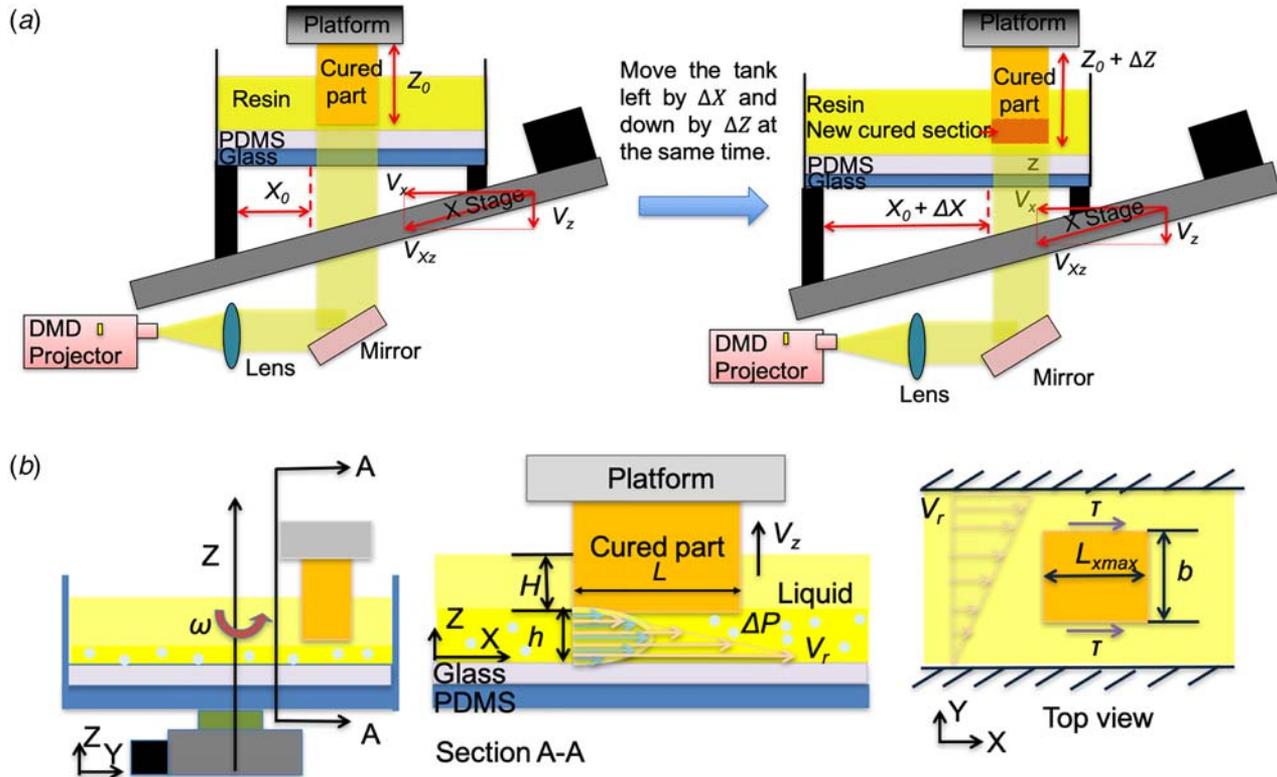
Fig. 3 An illustration of the material recoating with two-way movements: (a) an illustration of the recoating process with two-way movements and (b) an illustration of resin recoating of continuous resin flow with two-way movements

through the channel between the cured layers and the PDMS surface, the viscosity of the liquid resin increases exponentially during the continuous photocuring process [32]. To illustrate the refilling problem, we analyzed the resin refilling velocity in the X direction v_r. We set angular velocity as ω for the rotation stage. By using additional boundary conditions, the velocity of the resin flow in the X direction V_x can be derived as the following [36,37]:

$$v_r = \frac{\Delta p}{\mu e^k L}\left[\left(\frac{h}{2}\right)^2 - \left(z - \frac{h}{2}\right)^2\right] + \omega y - \frac{\omega yz}{h} \quad (8)$$

In the MVP-SL$_{CRF}$ process, the approximate flow rate of liquid resin under the cured part with square section area L^2 can be predicted as follows:

$$Q = \int_{y_0-\frac{L}{2}}^{y_0+\frac{L}{2}} dy \int_0^h \frac{\Delta p}{\mu e^k L}\left[\left(\frac{h}{2}\right)^2 - \left(z - \frac{h}{2}\right)^2\right] + \omega y - \frac{\omega yz}{h} dz \quad (9)$$

In a unit time, the liquid resin that flows through the light projection area will be cured into solid. Therefore, we got the valid side length L of the cured part with sufficient resin as follows:

$$L = \left(\frac{Q}{V_z}\right)^{\frac{1}{2}} \quad (10)$$

Hence, after substituting Eq. (9) into Eq. (10), we rewrote the valid side length L of the cured part with sufficient resin as follows:

$$L_r = \frac{8h\omega y_0 + \left(64h^2\omega^2 y_0^2 - \frac{32\Delta p h^3}{3\mu e^k}\right)^{\frac{1}{2}}}{16V_z - h\omega} \quad (11)$$

Bases on Eq. (11), the valid side length L_r of the cured part would increase with the angular velocity ω. However, due to the sliding movement of the resin tank, the cured part will also suffer from a

viscous drag in the X direction, which makes microscale feature difficult to attach on the anterior portion of the built object. The shear stress τ in the continuous resin flow depends on the viscosity μ' and the speed v_r of the liquid flow as shown in the following equation [37,38]:

$$F_d = \mu' V_x A \quad (12)$$

At the same time, the maximum allowed force is represented by the maximum bending force for a beam [26]. The maximum bending force follows the equation:

$$F_B = \frac{\sigma_b \times L^3}{6Z_p} \quad (13)$$

where σ_b is the flexural strength (around 65 MPa for EnvisionTEC SI500), Z_p is the height of the built beam, and L is the length of the built beam. To avoid the damage of the built part caused by the viscous drag of the liquid flow, the share force should be smaller than the maximum bending force. Therefore, the velocity of the side movement can be calculated as follows:

$$V \le \frac{\sigma_b \times L^2}{12\mu' H Z_p} \quad (14)$$

Hence, the speed of the sliding movement should be set no large than the threshold; otherwise, the continuous building process will fail due to the large shear force. At the same time, the speed of the sliding movement should be set large enough to ensure sufficient resin flow for the mask video projection process.

3.3 Experimental Study of Parameter Setting. A rotary stage was integrated into the MVP-SL$_{CRF}$ process to generate the continuous liquid flow (refer to Fig. 3(b)). The design of experiment method was applied to optimize the parameter settings of the MVP-SL$_{CRF}$ process. The relationship between the side length of
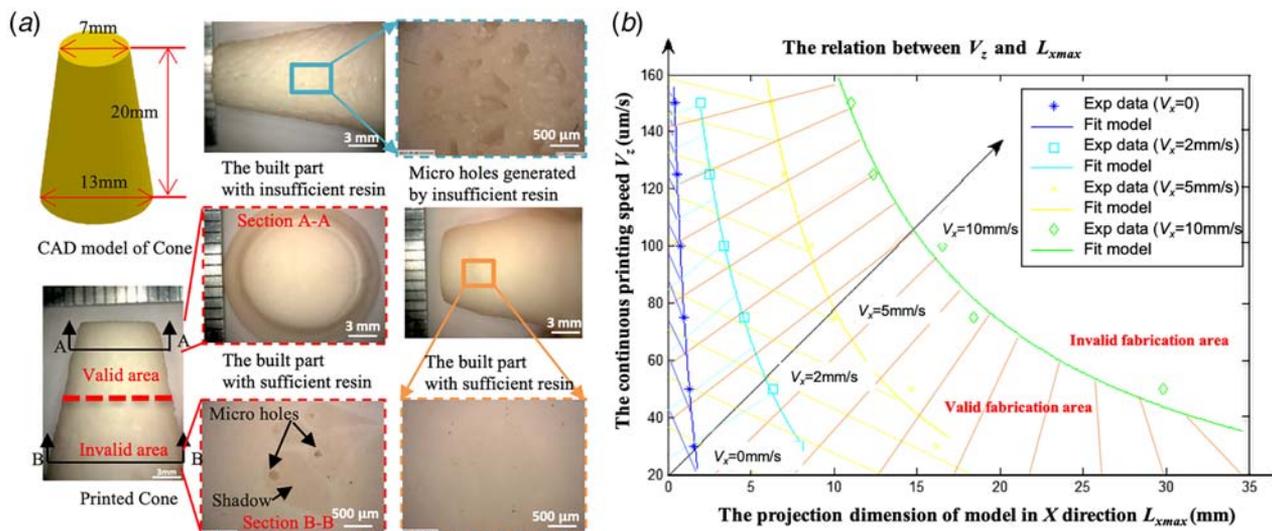
Fig. 4 (a) Fabrication results of the cones with side moving speed V_x and continuous printing speed $V_z = 100\ \mu$m/s and (b) the relative valid side length L of cured solid with sufficient resin versus the printing speed V_z and the side moving speed V_x

the valid cured part L, the moving speed of rotary stage V_x, and the continuous printing speed V_z were studied. In the continuous liquid flow, based on Eq. (11), the smallest moving speed of rotation speed V_z is determined by the maximum projection length of a built object in the X direction L_{xmax}. To verify this assumption, a set of experiments were designed to calibrate the required minimum moving speed V_x in the X direction in order to achieve sufficient resin refilling in the building area. A series of cones were fabricated whose diameters of the cross-sectional areas are gradually increased from 2 mm to 35 mm. We applied different moving speeds of the rotary stage V_x to fabricate the cones. Similar to the aforementioned study, if a built object has holes or shadows in the cross section of the built layers (refer to Fig. 4(a)), we considered that the moving speed V_x was not large enough to continuously refill the resin. In addition, a built part with bubbles in the cross-sectional area was also regarded as a failure for the continuous fabrication due to insufficient resin refilling. To overcome the fabrication defects, V_x was gradually increased to rebuild the part; when all bubbles and shadowing areas are eliminated, the value setting of V_x is considered to be located in the valid moving speed range for the MVP-SL$_{CRF}$ process. Experiments were repeated until the biggest section area of the cone part has been successfully fabricated (refer to Fig. 4(a)). When the setting of V_x is not large enough to cover the whole area, there will be a boundary on the surface of the built cones separating the cone into two regions, one side is void free and another is with voids. Hence, we can trace back to find the critical void-free curing section area A_x for certain moving speed V_x in the X direction.

By using this method, for a given continuous printing speed V_z, the critical moving speed V_x can be identified based on different maximum projection length (L_{xmax}). A set of experimental results have been performed following the trial-error method, as shown in Fig. 4(b). The grid area below the fitted line was the valid fabrication area regarding a given moving speed V_x. From Fig. 4(b), we can see that the valid fabrication area is increased dramatically with the increase of the side moving speed V_x for the same printing speed V_z. Based on the experimental data, we further fitted the mathematical model as shown in Eq. (15) to calculate the critical moving speed V_x in the X direction in order to successfully achieve the continuous liquid flow.

$$V_{xmin} = k_1 V_Z L_{xmax} - k_2 \frac{1}{L_{xmax}} \qquad (15)$$

where k_1 and k_2 are constants.

Sufficient resin refilling can be provided by the increased side movement speed; however, due to the viscosity of the liquid resin, a larger side moving speed also leads to an increased shear force. While the continuous fabrication of a large area has been enabled by speeding up the side movement, the small features in the object may be damaged due to a large shear force. To identify the valid maximum speed of the side movement, we fabricated several bars with different cross-sectional areas. Figure 5 shows the results of the fabricated objects with different moving speed V_x. As V_x increases beyond the appropriate value, the surface qualities of the 3D-printed objects become worse. Especially for thin shells, some portions of the fabricated objects are damaged by the shear force due to the viscous drag. We analyzed the experimental data and fitted the mathematical model to calculate the critical maximum speed for each projection length L_{xmin} in order to avoid the damage of thin shell features in the model, as shown in Eq. (16).

$$V_{xmax} = k_3 L_{xmin}^2 \qquad (16)$$

where k_3 is equal to 1.2539 for the material SI500 when the height Z_p of the built part is 30 mm.

Based on the designed experimental results, it can be observed that:

(1) When $V_x < V_{xmin}$, the object cannot be fabricated due to insufficient resin flow; when $V_x > V_{xmax}$, the object can be fabricated, but some small features will be damaged; when $V_{xmin} < V_x < V_{xmax}$, there is no damage or bubbles in the cross-sectional area of the built parts and the surface quality is smooth without layer stairs.
(2) By using the same printing speed V_z, the minimum moving speed V_x increases with the maximum projection dimension L_{xmax} of the built part in the X direction. The bigger printing speed V_z will require an increased minimum moving speed V_x for faster liquid resin refilling in order to fabricate objects with the same L_{xmax}. By applying the moving speed V_x in the X direction, the valid fabrication area could be increased by 15 times compared with the traditional MVP-SL process without the side movement (i.e., $V_x = 0$).
(3) It is found that when the dimensional L_{xmax} is in the range of 0 mm–1 mm and the 3D printing speed is slower than 100 μm/s, adding the side movement V_x is not needed since the liquid resin can completely refill the gap during the
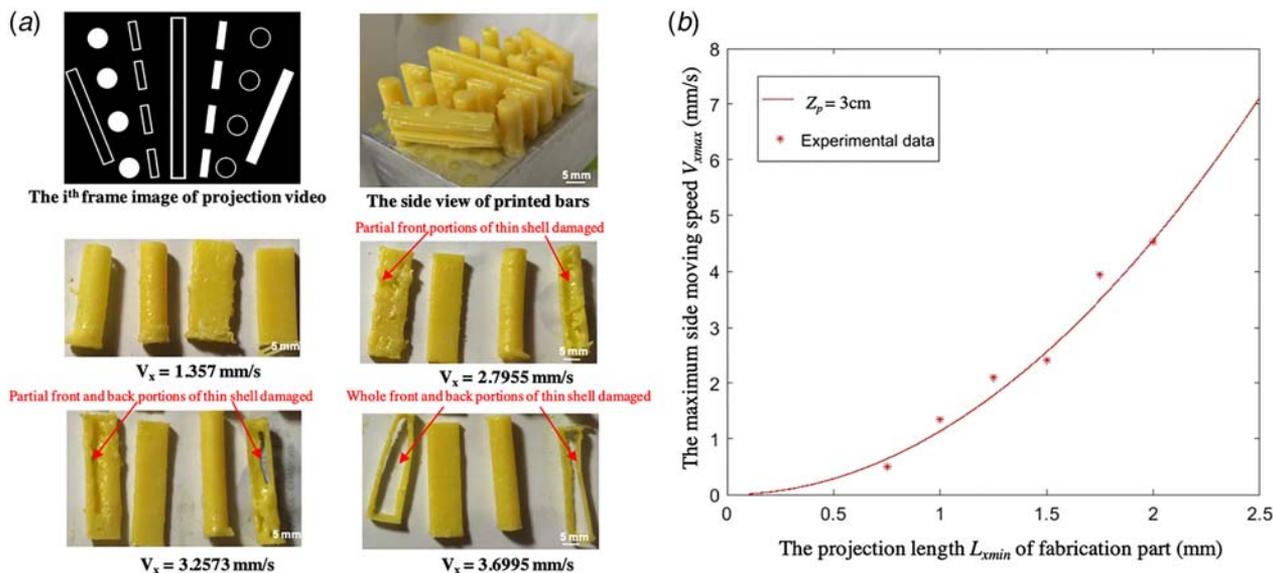
Fig. 5 (a) Fabrication results of shell and solid bars with different side moving speed V_x and (b) the relative maximum side moving speed V_{max} with the projection length L_{xmin} of the fabrication part

continuous movement of the Z stage and with $V_x = 0$. However, only driven by the gravity and the ambient air pressure, the valid fabrication area is small; hence, only microscale and mesoscale features can be fabricated with the PDMS film. In order to fabricate macroscale features, the minimum moving speed V_x in the X direction can be approximated by a fitted model, which was established by a set of calibration tests. For a solid model with a large cross section, V_z could reach 100 μm/s with V_x set at 10 mm/s.

(4) Theoretically, a solid model with large cross-sectional area can be successfully fabricated with sufficient resin refilling by increasing the moving speed V_x in the X direction. However, the flow of liquid resin when passing the printed part will have viscous drag. In addition, liquid resin will transfer from steady state to oscillating state when the speed of resin flow exceeds a critical point $\frac{5\mu}{L_{xmax}}$ [39]. The unstable oscillating has an impact on the surface quality of the backside of the printed part. To avoid the turbulence, the moving speed of V_x in the X direction cannot be increased to beyond a certain level, which can be determined by the Reynolds number of the resin flow [39].

4 Results and Discussion

A MVP-SL$_{CRF}$ prototype has been constructed to verify the developed continuous fabrication method. Our MVP-SL$_{CRF}$ prototype contains an optical system, a mechanical system, and a tank that can be continuously rotated. The optical system is composed of a light lamb, a DMD chip, and a set of optical lenses [26]. The power of the visible lamb used in our system is 3000 lumens, and the DMD chip (Texas Instruments, TX) has a resolution of 1024 ×768. There are two stages in the MVP-SL$_{CRF}$ mechanical system. A precise linear stage from Aerotech, Inc. (Pittsburgh, PA) was used as the elevator for the continuous movement of the platform in the Z-axis. A fast rotary stage from Velmex, Inc. (Bloomfield, NY) was applied to rotate the tank for achieving the continuous liquid flow. The resin tank was a flat and clear glass Petri dish with 2 mm thick PDMS coating on the bottom [26]. A software testbed for the continuous two-way movement has been developed using c++ language with Microsoft Visual Studio C++ compiler [26,28]. The testbed integrates geometric shape slicing, mask video generation, video loading and projection, and motion control. It also synchronizes the video projection with the rotary movement and the Z linear movement.

Various tests have been performed to verify the capability of the developed MVP-SL$_{CRF}$ process in fabricating geometries with different cross-sectional areas. The experimental results have demonstrated that the presented AM process can continuously fabricate CAD models using high frame rate videos; hence, the printing process is ultrafast, and all the models can be fabricated in minutes instead of hours. In addition, the fabricated 3D objects have desired accuracy and surface smoothness without the stair-stepping effect.

4.1 Experimental Result. A set of CAD models with different geometric complexity were fabricated using the MVP-SL$_{CRF}$ prototype with G+ (white) from MakerJuice Labs and Perfatory^{TM} SI500 (yellow) from EnvisionTEC, Inc. (Ferndale, MI). The curing characteristics of the two resins are slightly different, and the viscosity of G+ is half of that of SI500. Table 2 shows the parameter settings that were used in the preformed tests. The CAD models and the final fabrication results are shown in Figs. 6–9. The triangle numbers of these STL files ranges from several hundreds to 1.2 million (refer to Table 2).

In computing the mask images to create the projection videos, two kinds of slicing thicknesses (1 μm and 5 μm) were tested in our experiments. In the fabrication of Yosemite bear and lamp shade models, videos were projected at the frame rate of 75 fps with the continuous speed V_z of 75 μm/s. During the fabrication process of other models, the speeds were set as 100 μm/s and

Table 2 Parameters of MVP-SL$_{CRF}$

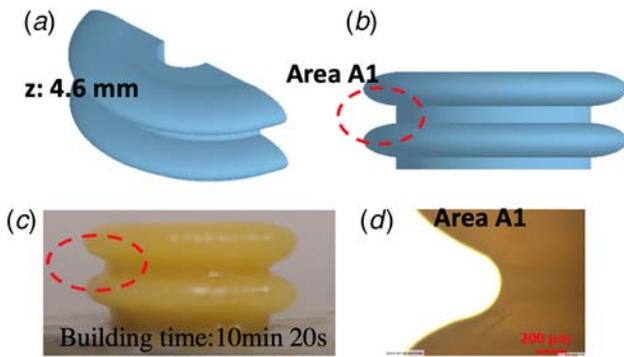| Model	Height (mm)	Tri No.	V_x (mm/s)	V_z (μm/s)	Video FPS (Hz)	T (min)
Nests ball	30.4	28,800	1.0	120	75	5.02
Hear aid	22.9	32,762	3.1	100	20	4.0
Yosemite bear	65.1	289,728	1.0	75	75	15.9
Lamp shade	26.0	1380	1.5	75	20	5.78
Umbrella-shaped shell	25.4	65,825	1.5	100	20	4.19
Cylinder	25.4	1980	1.0	120	24	4.53

Fig. 6 A freeform surface fabrication by the MVP-SL$_{CRF}$ process: (a) and (b) CAD model of freeform surface, (c) the surface quality of the printed freeform surface under microscope, and (d) side view of microscope image of area A1
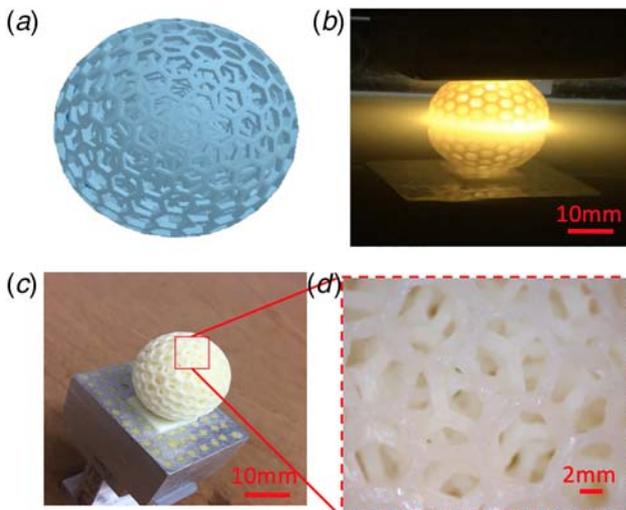

Fig. 7 Printed *Eight Nested ball* using MVP-SL$_{CRF}$ process: (a) CAD model of *Eight Nested ball*, (b) screenshot during the printing process, (c) top view of the printed ball using MVP-SL$_{CRF}$ process, and (d) the surface quality of printed balls under the microscope
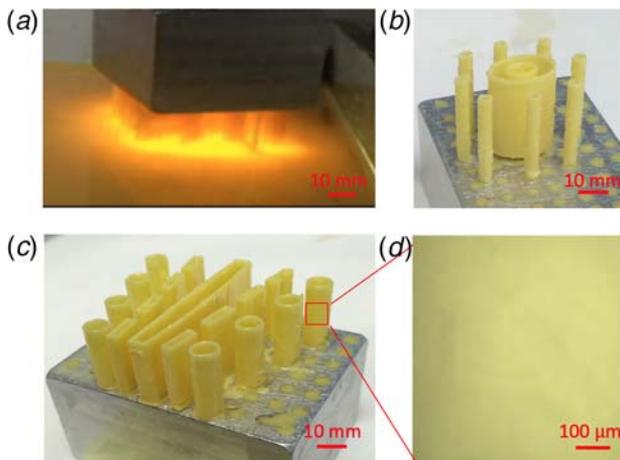

Fig. 8 Printed *macro-shell* using MVP-SL$_{CRF}$ process: (a) the continuous projection light, (b) side view of printed cylinders using MVP-SL$_{CRF}$ process, (c) fabricated *umbrella-shaped shell* by MVP-SL$_{CRF}$, and (d) microscope image of the printed surface of *umbrella-shaped shell* using the MVP-SL$_{CRF}$

120 μm/s (refer to Table 2). In all the tests, the moving speed V_x was calculated based on the maximum projection length of the object L_{xmax}. For each layer with an entire solid cross-sectional area (e.g., the model of a solid wall), the X direction moving speed reached 3.5 mm/s. Because the cross-sectional area of a shell is not as large as a solid one, the moving speed in the X direction (V_x) is much smaller when fabricating shell structures. From the microscope images of Figs. 6–8, the printing quality is improved with smooth surfaces using a smaller V_x. By controlling the side moving speed V_x based on the valid fabrication area, the macroscale features can be continuously printed with an ultrafast fabrication speed.

4.2 Comparison With the Layer-Based SL Process. We compared the fabrication time and surface quality of the MVP-SL$_{CRF}$ process and the layer-based MIP-SL process. The three models shown in Fig. 9 were built by the MVP-SL$_{CRF}$ process, which only took less than 1/5 time as required by the layer-based MIP-SL process. The hearing aid shell model only requires 4 min to build; in comparison, since it has 230 layers if using 0.1 mm layer thickness, it would cost ~60 min for a commercial ultra machine from EvnistionTec (Ferndale, MI) (~16 s per layer) and ~20 min using the fast MIP-SL process (~5.2 s per layer) [26]. The comparison results of other test cases were similar. In general, the fabrication time by MVP-SL$_{CRF}$ was 75–120 μm per second. In addition to the fabrication efficiency, the surface quality is also significantly improved using the MVP-SL$_{CRF}$ process. The continuous mask video projection reduced the stair-stepping effect, and the surfaces turn to be much smoother. As shown in Fig. 9(c), the layer stair-stepping effect was obvious in the 3D object fabricated by the MIP-SL process using 0.1 mm layer thickness, while the stair-stepping effect was not observed on the surface of the object built by the MVP-SL$_{CRF}$ process even under a microscope.

5 Conclusion

In this paper, a novel MVP-SL$_{CRF}$ has been presented. We demonstrated that the new additive manufacturing process can achieve a fast building speed using an actively controlled resin feeding method. The MVP-SL$_{CRF}$ process was shown to have a fabrication speed that is five to ten times faster than that of the layer-based MIP-SL process. We discussed the challenging issues in the continuous fabrication-based MVP-SL process including resin refilling and photo curing performance. Related mathematical models have been established. Based on them, we discussed how our approach can address the identified issues in MVP-SL$_{CRF}$. The system design and related parameter settings to achieve an ultrafast fabrication speed have been presented. The relationship between the process parameters and the building quality has been discussed. Finally, the fabrication results have demonstrated that the MVP-SL$_{CRF}$ process can fabricate 3D objects with various geometric features within minutes, and the surface quality of the built objects is improved with no obvious stair-stepping effect.

The presented MVP-SL$_{CRF}$ is simple and cost friendly with significant advantages on fabricating CAD models with large cross-sectional areas. Although a PDMS film was used in our prototype, we believe that the developed MVP-SL$_{CRF}$ process can also be extended to other MVP-SL processes such as CLIP. With a much larger oxygen inhibition layer, we expected that the continuous two-way movement as discussed in this paper would lead to a further increased fabrication speed for geometric shapes with larger cross-sectional areas.

The newly developed MVP-SL$_{CRF}$ also brings some new problems such as viscous drag to small features. We are also developing new techniques that can modulate the continuous resin flow pattern in MVP-SL$_{CRF}$ to address geometric shapes with large cross-sectional areas. Finally, a layer-less AM process that can continuously build 3D objects without layer-based recoating presents a potential solution for many emerging industry applications.
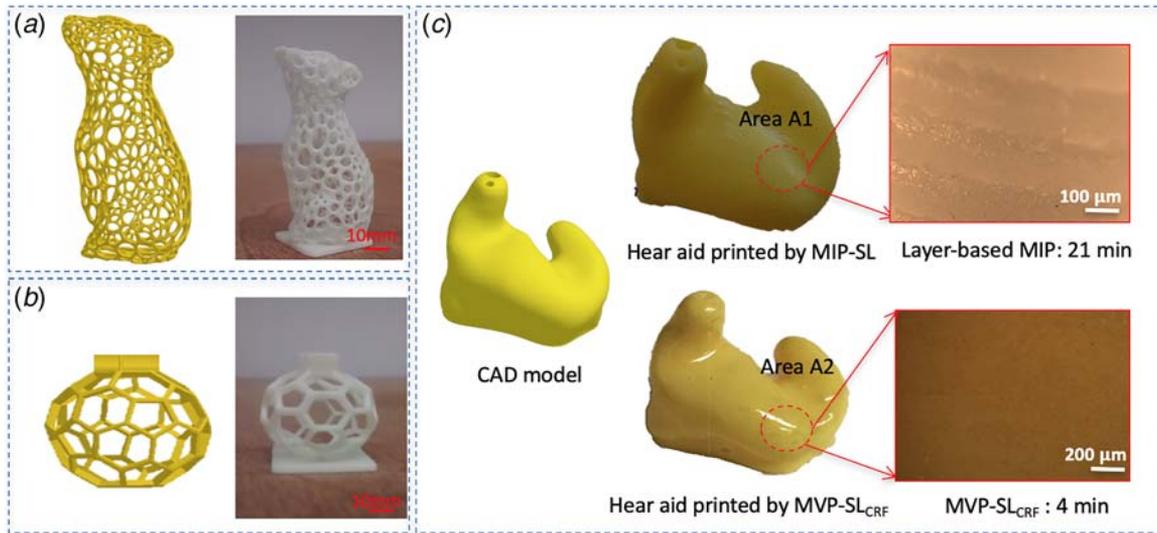
Fig. 9 Printed *Yosemite bear* and *lampshade* using MVP-SL$_{CRF}$ process: (*a*) CAD model of *Yosemite bear* and side view of the printed bear using the MVP-SL$_{CRF}$ process, (*b*) the CAD model of *lampshade* and side view of the printed lampshade using the MVP-SL$_{CRF}$ process, and (*c*) comparison of the fabrication results for a hearing aid shell using MIP-SL and MVP-SL process

We hope our research will inspire more layer-less AM process developments to address the fabrication demands for AM technology in future.

Nomenclature

H = the oxygen inhibition layer thickness
h = the gap height between the cured part and PDMS
k = the constant indicates the material energy
r = the radius of the rotation tank
t = the liquid filling time
z = the position away from the tank
A = cross-sectional area of cured part
H = the height of resin
L = the projection length of a built object in the X direction
S = the side length of cured part
$\vec{F}$ = body forces
$\tilde{\tilde{\tau}}$ = stress tensor
k_1 = the constant
k_2 = the constant
k_3 = the constant
k_z = the printing speed ratio
v_r = the refilling speed of resin
C_d = the cure depth of material
D_p = the light penetration depth
E_c = the critical energy of exposure
E_{max} = the energy of light exposure
F_b = the bending force
L_r = the valid side length of fabrication area with sufficient resin refilling
L_{xmax} = the maximum projection length of a built object in the X direction
L_{xmin} = the minimum projection length of a built object in the X direction
V_x = the speed of side movement
V_z = the printing speed in the z direction
Z_p = the total height of cured object
Δp = the pressure difference
∇p = pressure gradient
μ = the viscosity of resin
ρ = the density of resin
σ = the flexural strength
τ = the shear stress
ω = the angular velocity of rotary tank

References

[1] Gao, W., Zhang, Y., Ramanujan, D., Ramani, K., Chen, Y., Williams, C. B., Wang, C. C. L., Shin, Y. C., Zhang, S., and Zavattieri, P. D., 2015, "The Status, Challenges, and Future of Additive Manufacturing in Engineering," Comput. Aided Des., **69**(C), pp. 65–89.

[2] Lu, L., Tang, X., Hu, S., and Pan, Y., 2018, "Acoustic Field-Assisted Particle Patterning for Smart Polymer Composite Fabrication in Stereolithography," 3D Print. Addit. Manuf., **5**(2), pp. 151–159.

[3] Yang, Y., Song, X., Li, X., Chen, Z., Zhou, C., Zhou, Q., and Chen, Y., 2018, "Recent Progress in Biomimetic Additive Manufacturing Technology: From Materials to Functional Structures," Adv. Mater., **30**(36), pp. 1706539.

[4] Leung, Y. S., Kwok, T. H., Li, X., Yang, Y., Wang, C. C., and Chen, Y., 2018, "Challenges and Status on Design and Computation for Emerging Additive Manufacturing Technologies," ASME J. Comput. Inf. Sci. Eng., **19**(2), p. 021013.

[5] Li, X., Xie, B., Jin, J., Chai, Y., and Chen, Y., 2018, "3D Printing Temporary Crown and Bridge by Temperature Controlled Mask Image Projection Stereolithography," Proc. Manuf., **26**, pp. 1023–1033.

[6] Pan, Y., and Chen, Y., 2015, "Smooth Surface Fabrication Based on Controlled Meniscus and Cure Depth in Microstereolithography," ASME J. Micro Nano-Manuf., **3**(3), p. 031001.

[7] Pan, Y., Zhao, X., Zhou, C., and Chen, Y., 2012, "Smooth Surface Fabrication in Mask Projection Based Stereolithography," J. Manuf. Process, **14**(4), pp. 460–470.

[8] Li, X., Baldacchin, T., Song, X., and Chen, Y., 2016, "Multi-Scale Additive Manufacturing: An Investigation on Building Objects With Macro-, Micro- and Nano-Scales Features," 11th International Conference on Micro Manufacturing, Irvine, CA, Mar. 29, p. 96.

[9] Huang, S. H., Liu, P., Mokasdar, A., and Hou, L., 2013, "Additive Manufacturing and Its Societal Impact: A Literature Review," Int. J. Adv. Manuf. Technol., **67**(5–8), pp. 1191–1203.

[10] Yazdi, A. A., Popma, A., Wong, W., Nguyen, T., Pan, Y., and Xu, J., 2016, "3D Printing: An Emerging Tool for Novel Microfluidics and Lab-on-a-Chip Applications," Microfluid. Nanofluid., **20**(3), p. 50.

[11] Jo, K. H., Lee, S. H., and Choi, J. W., 2018, "Liquid Bridge Stereolithography: A Proof of Concept," Int. J. Precis. Eng. Manuf., **19**(8), pp. 1253–1259.

[12] Park, I. B., Ha, Y. M., and Lee, S. H., 2011, "Dithering Method for Improving the Surface Quality of a Microstructure in Projection Microstereolithography," Int. J. Adv. Manuf. Technol., **52**(5–8), pp. 545–553.

[13] Pan, Y., and Chen, Y., 2016, "Meniscus Process Optimization for Smooth Surface Fabrication in Stereolithography," Addit. Manuf., **12**(B), pp. 321–333.

[14] Chen, Y., Zhou, C., and Lao, J., 2011, "A Layerless Additive Manufacturing Process Based on CNC Accumulation," Rapid Prototyping J., **17**(3), pp. 218–227.

[15] Pan, Y., Zhou, C., Chen, Y., and Partanen, J., 2014, "Multitool and Multi-Axis Computer Numerically Controlled Accumulation for Fabricating Conformal Features on Curved Surfaces," J. Manuf. Sci. Eng., **136**(3), p. 031007.

[16] Tumbleston, J. R., Shirvanyants, D., Ermoshkin, N., Janusziewicz, R., Johnson, A. R., Kelly, D., Chen, K., Pinschmidt, R., Rolland, J. P., Ermoshkin, A., and Samulski, E. T., 2015, "Continuous Liquid Interface Production of 3D Objects," Science, **347**(6228), pp. 2397.

[17] O'Bryan, C. S., Bhattacharjee, T., Hart, S., Kabb, C. P., Schulze, K. D., Chilakala, I., Sumerlin, B. S., Sawyer, W. G., and Angelini, T. E., 2017, "Self-Assembled Micro-Organogels for 3D Printing Silicone Structures," Sci. Adv., **3**(5), p. e1602800.

[18] Bhattacharjee, T., Zehnder, S. M., Rowe, K. G., Jain, S., Nixon, R. M., Sawyer, W. G., and Angelini, T. E., 2015, "Writing in the Granular gel Medium," Sci. Adv., **1**(8), p. e1500655.

[19] Günther, D., Heymel, B., Franz Günther, J., and Ederer, I., 2014, "Continuous 3D-Printing for Additive Manufacturing," Rapid Prototyping J., **20**(4), pp. 320–327.

[20] Li, X., and Chen, Y., 2017, "Micro-Scale Feature Fabrication Using Immersed Surface Accumulation," J. Manuf. Proc., **28**, pp. 531–540.

[21] He, H., Yang, Y., and Pan, Y., 2019, "Machine Learning for Continuous Liquid Interface Production: Printing Speed Modelling," J. Manuf. Systems, **50**, pp. 236–246.

[22] Song, X., Pan, Y., and Chen, Y., 2015, "Development of a Low-Cost Parallel Kinematic Machine for Multidirectional Additive Manufacturing," J. Manuf. Sci. Eng., **137**(2), p. 021005.

[23] Yang, Y., Li, X., Zheng, X., Chen, Z., Zhou, Q., and Chen, Y., 2018, "3D-Printed Biomimetic Super-Hydrophobic Structure for Microdroplet Manipulation and Oil/Water Separation," Adv. Mater., **30**(9), p. 1704912.

[24] Li, X., Yang, Y., and Chen, Y., 2017, "Bio-Inspired Micro-Scale Texture Fabrication Based on Immersed Surface Accumulation Process," Proceedings of the World Congress on Micro and Nano Manufacturing Conference (WCMNM), Kaohsiung, Taiwan, Mar. 27–30, pp. 33–36.

[25] He, H., Pan, Y., Feinerman, A., and Xu, J., 2018, "Air-Diffusion-Channel Constrained Surface Based Stereolithography for Three-Dimensional Printing of Objects With Wide Solid Cross Sections," J. Manuf. Sci. Eng., **140**(6), p. 061011.

[26] Pan, Y., Zhou, C., and Chen, Y., 2012, "A Fast Mask Projection Stereolithography Process for Fabricating Digital Models in Minutes," ASME J. Manuf. Sci. Eng., **134**(5), p. 051011.

[27] Jin, J., Yang, J., Mao, H., and Chen, Y., 2018, "A Vibration-Assisted Method to Reduce Separation Force for Stereolithography," J. Manuf. Proc., **34**(PB), pp. 793–801.

[28] Zhou, C., Chen, Y., Yang, Z., and Khoshnevis, B., 2013, "Digital Material Fabrication Using Mask-Image-Projection-Based Stereolithography," Rapid Prototyping J., **19**(3), pp. 153–165.

[29] Song, X., Chen, Y., Lee, T. W., Wu, S., and Cheng, L., 2015, "Ceramic Fabrication Using Mask-Image-Projection-Based Stereolithography Integrated With Tape-Casting," J. Manuf. Proc., **20**, pp. 456–464.

[30] Zhou, C., Chen, Y., Yang, Z. G., and Khoshnevis, B., 2011, "Development of multi-material mask-image-projection-based stereolithography for the fabrication of digital materials," Annual solid freeform fabrication symposium, Austin, TX, Aug. 12–14, pp. 65–80.

[31] Dendukuri, D., Pregibon, D. C., Collins, J., Hatton, T. A., and Doyle, P. S., 2006, "Continuous-Flow Lithography for High-Throughput Microparticle Synthesis," Nat. Mater., **5**(5), p. 365.

[32] Odian, G., 2004, Principles of Polymerization, John Wiley & Sons, New York.

[33] Jacobs, P. F., 1992, Rapid Prototyping & Manufacturing: Fundamentals of Stereolithography, Society of Manufacturing Engineers, Southfield, MI.

[34] Batchelor, G. K., 2000, An Introduction to Fluid Dynamics, Cambridge University Press, Cambridge, UK.

[35] Moser, R. D., Moin, P., and Leonard, A., 1983, "A Spectral Numerical Method for the Navier-Stokes Equations with Applications to Taylor-Couette Flow," J. Comput. Phys., **52**(3), pp. 524–544.

[36] Larson, R. G., Shaqfeh, E. S., and Muller, S. J., 1990, "A Purely Elastic Instability in Taylor–Couette Flow," J. Fluid Mech., **218**, pp. 573–600.

[37] Wereley, S. T., and Lueptow, R. M., 1999, "Velocity Field for Taylor–Couette Flow with an Axial Flow," Phys. Fluids, **11**(12), pp. 3637–3649.

[38] Santilli, R. M., 2012, Foundations of Theoretical Mechanics II: Birkhoffian Generalizations of Hamiltonian Mechanics, Springer Science & Business Media, New York.

[39] Amalia, E., Moelyadi, M. A., and Ihsan, M., 2018, "Effects of Turbulence Model and Numerical Time Steps on Von Karman Flow Behavior and Drag Accuracy of Circular Cylinder," J. Phys. Conf. Ser., **1005**(1), pp. 012012.